

Probability and causes of shoal margin collapses in a sandy estuary

Wout M. van Dijk ^{*1}, Dick R. Mastbergen², Geeralt A. van den Ham³, Jasper R.F.W. Leuven¹,
and Maarten G. Kleinhans¹

¹Department of Physical Geography, Faculty of Geosciences, Utrecht University, Utrecht, The Netherlands

²Department of Ecosystems and Sediment Dynamics, Deltares, Delft, The Netherlands

³Department of Geo-engineering, Deltares, Delft, The Netherlands

May 9, 2017

Abstract

Channel bank failure and collapses of shoal margins due to flow slides have been recorded in Dutch estuaries for the past 200 years because these frequently caused dike failure. Current predictions lack forecasting capabilities, because they were validated and calibrated for historic data of cross-sections in specific systems, allowing local hindcast rather than location and probability forecasting. The objectives of this study are to investigate where on shoal margins the collapses typically occur and what shoal margin collapse geometries and volumes are, such that we can predict their occurrence. We identified shoal margin collapses from bathymetry data by analyzing DEMs of Difference (DoD) of the Western Scheldt for the period 1959-2015. We used the bathymetry data to determine the relative slope height and angle and applied these variables in a shoal margin collapse predictor. We found 299 collapses along 300 km of shoal margin boundaries, meaning more than 5 collapses occur on average per year. The average shoal margin collapse body is well approximated by a 1/3 ellipsoid shape, covers on average an area of 34,000 m², and has an average volume of 100,000 m³. Shoal margin collapses occur mainly at locations where shoals take up a proportionally larger area than average in the cross-section of the entire estuary, and occur most frequently where lateral shoal margin displacement is low. An earlier method to predict the probability of shoal margin collapse predicts generally low probabilities of shoal margin collapses, but recalibration to a normalized slope height and angle from our analysis increased the probabilities. A receiver operating characteristic curve shows that the forecasting method predicts the shoal margin collapse location well. We conclude that the locations of the shoal

*W.M.vanDijk@uu.nl

margin collapses are well predicted by the variation in conditions of the relative slope height and angle within the Western Scheldt, and likely locations are laterally relatively stable shoal margins.

Keywords: Shoal margin collapse; Flow slide; Shoal morphodynamics; Western Scheldt; Forecasting tool; Estuaries

1 Introduction

Channel bank failures and collapses of shoal margins (flow slides) have been recognized in estuaries and rivers around the world (Coleman, 1969; Laury, 1971; Silvis and De Groot, 1995; Torrey, 1995; Dunbar et al., 1999; Van den Berg et al., 2002; Beinssen et al., 2014). The style and development of failure processes and collapses is controlled by flow conditions, slope geometry, clay layers and the void ratio (Stoutjesdijk et al., 1998; Olson and Stark, 2002; Deangeli, 2007; Van den Ham et al., 2014). The morphological and societal importance of shoal margin collapses are considerable: typically collapses occur up to 1 M m^3 in the Western Scheldt (Figure 1) that approach annually dredged volumes of 10 M m^3 (Wang and Winterwerp, 2001; Dam et al., 2007; Jeuken and Wang, 2010). Moreover, collapses often threatened levees and stability of vital constructions such as the Eastern Scheldt storm surge barrier (Stoutjesdijk et al., 2012). Shoal margin collapses in the Western Scheldt are a significant problem as the fairway requires a certain width-to-depth ratio to the harbor of Antwerp. Numerical morphodynamic models, e.g., Delft3D, ignore channel-shoal margin collapses and inadequately predict gentle slope processes and mud settling. We would like to investigate their effects on large-scale dynamics of channels and shoals and explore dredging and dumping scenarios that optimize cost and benefit habitat surface area and quality. However, before including the process of shoal margin collapse into a numerical morphodynamic model, we must first understand the spatial pattern, organization and geometries of shoal margin collapses in order to simulate shoal margin collapses.

Two fundamentally different types of underwater shoal margin collapses occur: rapid flow slides due to liquefaction and slow retrogressive flow slides due to breaching (Van den Berg et al., 2002; Van den Ham et al., 2014; Mastbergen et al., 2016). Flow slides occur at lower angles and displaces much more sediment over much larger distances than the well-known classic (river) bank

53 shear failure that is followed by a slump or slide over a short distance (Simon and Collinson, 2002;
54 Kleinhans et al., 2009). Besides these shoal margin collapses often occur at the inner side of a
55 bend instead channel bank failure that occurs at the outer side. The general failure mechanisms
56 of channel banks proceed from undercutting by sand removal on the transverse bed slope at the
57 bank toe. A liquefied flow slide, however, entails the sudden loss of strength of loosely packed
58 saturated sand or silt, resulting in a sudden collapse (Lowe, 1976) but has never been observed in
59 estuaries. Destabilization commonly occurs due to seepage of water out of the bank (Xie et al.,
60 2009) by increasing pore water pressure but also a larger part of the slope is above the phreatic line,
61 which increases the shear stresses in the submerged part. This is often observed in falling stage
62 in rivers (Simon and Collinson, 2002) and falling tides (Christian et al., 1998). Breaching occurs
63 when a steep scarp releases fine compacted sediment particle-by-particle or in thin slabs. Contrary
64 to liquefied flow slides, breaching sediment is densely packed so that water has to infiltrate and
65 increase pore space, i.e., dilatancy, before it can flow, which is slower for finer sand. The under-
66 pressurized sand therefore maintains a much steeper slope than the angle of repose that slowly
67 retrogresses defined by permeability. The breaching process continues for hours as observed in
68 submarine canyons (Inman et al., 1976), river banks (Coleman, 1969; Torrey, 1995) and estuaries
69 (Wilderom, 1961, 1964, 1968, 1973; Silvis and De Groot, 1995; Van den Berg et al., 2002). These
70 slow flow slides require only a minor trigger (Van Rhee and Bezuijen, 1998), which explains the
71 rather erratic nature of these events in time and space.

72 The processes of liquefaction and breaching requires various conditions (Van den Ham et al.,
73 2014). Liquefied flow slides and breaching occur both at sufficiently high and steep slopes. Lique-
74 faction, however, requires loosely packed, non-lithified, and water-saturated sand or silt, whereas
75 breaching requires the presence of a sufficiently large body of densely packed fine sand or silt.
76 These processes are included in two models as follows. The HMBreach model allows assessing
77 the sensitivity of a submerged slope with given geometry and sand properties to breaching, by
78 calculating the minimum size of the initial breach for it to trigger a self-accelerating breachflow
79 (Mastbergen and Van den Berg, 2003; Mastbergen, 2009). The SLIQ2D model calculates whether
80 in a submerged slope a static liquefaction may occur or not, based on the slope geometry, the rel-

81 ative density and the material properties of the sand or silt (Stoutjesdijk, 1994; Stoutjesdijk et al.,
82 1998). Van den Ham et al. (2014) argued that these theoretical liquefaction and breaching models
83 quantify the relative influences of channel geometry and soil parameters but the reliability of the
84 estimated probability remains limited. Therefore, Van den Ham et al. (2014) proposed a semi-
85 empirical model that predicts the probability of shoal margin collapses. This predictor includes
86 an empirical factor based on the frequency of historical flow slides in Zeeland (Wilderom, 1979).
87 The method of Van den Ham et al. (2014) is mainly applied for hindcasting, i.e., to test by observ-
88 ing whether it would have correctly predicted a bank collapse, and to anticipate the probability of
89 channel bank collapses per km per year, but has not been tested on spatial maps for the occurrence
90 of shoal margin collapses. However, a forecasting method is needed before we can investigate the
91 effects of shoal margin collapses on large-scale dynamics of channels.

92 Here we study shoal margin collapses based on bed elevation data of the Western Scheldt for
93 the period 1959-2015. The tidal flats of the Western Scheldt, including the shoals, have increased
94 in height and steepness over the past decades (De Vet et al., 2017), leading to conditions that are
95 favorable for new collapses and stressing the need for a predictor of locations, probabilities and
96 dimensions. The objectives of this study are to identify spatial patterns of shoal margin collapses
97 and determine their geometries and dimensions, and modify the method of Van den Ham et al.
98 (2014) to predict shoal margin collapses, and assess the accuracy of this prediction with observed
99 shoal margin collapse locations. In this paper, we first give a detailed description of the study area
100 and describe the methods and data that are used for the spatial pattern analysis and geometries
101 of shoal margin collapses. Then, we present the map of shoal margin collapses, shoal geometry
102 distributions and probability of occurrence in the Western Scheldt. Finally, we modify the applied
103 forecasting method, and explore its potential implications for numerical models.

104 **2 Study Area**

105 For reasons of data availability this study focus on the Western Scheldt, which is located in the
106 southwestern part of the Netherlands and is the seaward section (60 km) of the tide-dominated
107 Scheldt estuary that is 200 km long and stretches up to Gent in Belgium. The Western Scheldt is

108 characterized as a multiple channel system, with a well-developed system of channels and shoals.
109 It has on average a trumpet-shaped geometry and covers an area of about 370 km². The main
110 driving force of the system is the tide. From the mouth of the estuary to the Dutch/Belgian border,
111 the tidal range increases from 3.5 m to 5 m (Jeuken, 2000). The tidal prism at the mouth is about 1
112 billion m³, whereas the yearly-averaged river discharge of the Scheldt into the Western Scheldt is
113 a negligible 120 m³/s, causing the estuary to be well mixed (Cancino and Neves, 1999; De Vriend
114 et al., 2011). Relative fine sediment is found in the estuary: median grain size D_{50} of the channel
115 bed varies between about 150 μm and 300 μm , whereas sediment at the higher parts of the shoals
116 is generally smaller than 200 μm . Additionally, >10% of the intertidal areas contains dominantly
117 mud.

118 The Western Scheldt provides access to various harbors, of which the port of Antwerp (Bel-
119 gium) is the largest. Shoal margin collapses impact the fairway as sediment deposits into the
120 channel and affects the width and depth. Channel bank failures have been recorded in the Western
121 Scheldt and Eastern Scheldt estuary for the past 200 years. Between the 1800s and 1970s more
122 than 448 large failures with sediment volumes up to a million cubic meters were documented in
123 soundings of the Western Scheldt (Figure 2A, Wilderom, 1961, 1964, 1968, 1973, 1979). Besides
124 the identification of the large failures, Wilderom (1979) also identified locations that are suscepti-
125 ble to shoal margin collapses (Figure 2A, Wilderom, 1972). Over the years, especially since the
126 completion of the Delta works in 1987, bank protection measures were implemented to protect the
127 outer channel banks and dikes of the Western Scheldt for new failures (Figure 2B). These mea-
128 sures, including periodical maintenance, appeared so effective that such large bank collapse no
129 longer occurred. On the other hand, the tidal flats and the shoal margins are not essential for flood
130 protection so they are not protected and collapses have continued. The tidal flats in the Western
131 Scheldt, including the shoals, have increased in height and steepness over the past decades (De Vet
132 et al., 2017), partially as a result of the protection works (Wilderom, 1972), but also due to more
133 recent dredging and deepening. This results in conditions that are favorable for new collapses and
134 stress the need for a predictor of locations, probabilities and dimensions, whereas in the Eastern
135 Scheldt the tidal flats and shoal margins decrease in height (De Vet et al., 2017) because of the

136 reduced tidal range as result of the installation of the Storm Surge Barrier in 1987.

137 **3 Methods**

138 This paper evaluates the occurrence of shoal margin collapses in the Western Scheldt, particularly
139 on characteristic geometries of the collapsed shoal margin, the spatial distribution of shoal margin
140 collapses, and the underlying conditions for the shoal margin collapses. To establish shoal margin
141 collapse locations bathymetry data, so-called 'Vaklodingen', of the Western Scheldt are acquired
142 for the period 1959-2015. After visual identification of shoal margin collapses, the collapsed area
143 and volume as well as the spatial distribution are calculated. The bathymetry data are then used
144 to modify a shoal margin collapse predictor and the accuracy of the assessment is evaluated by a
145 Receiver Operating Characteristic (ROC) curve.

146 **3.1 Identification shoal margin collapses**

147 Shoal margin collapses were identified from existing digital elevation models. Digital elevation
148 models for the Western Scheldt came from bathymetry data with a grid resolution of 20x20 m
149 that were measured by Rijkswaterstaat and the Flemish government for the period 1959-2015 (see
150 example Figure 2A). This dataset combines single beam measurements at 100/200 m transects
151 extended with GPS Real-Time Kinematic (RTK) measurements on top of the tidal flats (also see
152 De Vet et al., 2017). Since 2001, the dry parts of the estuaries were measured with the Light
153 Detection and Ranging (LiDAR) technique, of which data was included in the bathymetry. The
154 vertical accuracy of the bathymetry data for the 20x20 m grid was estimated at 50 cm (2σ) for the
155 single beam and RTK data (Wiegmann et al., 2005). The accuracy improved for the LiDAR data,
156 approximately 30 cm (2σ). Because of the distance between transects some highs and lows are
157 not detected for the single beam measurements, which means that collapses up to 200 m between
158 consecutive transects are not visible but otherwise collapses larger than 400 m² could be detected.
159 Shoal margin collapses in the Western Scheldt were identified from produced slope maps, slope
160 difference maps, and DEMs of Difference (DoD) for consecutive years from 1960-2015. The re-
161 covery of the tidal flat of Walsoorden collapse of 2014 was monitored in the framework of the

162 Dutch-Flemish Western Scheldt monitoring program (Mastbergen and Schrijvershof, 2016) and
 163 data were analyzed to identify number and frequency of so far unnoticed shoal margin collapses in
 164 this area in the period 2000-2015 (VBA, 2016). We used similar criteria as VBA (2016) to identify
 165 shoal margin collapses, which were; (i) focused on local erosion phenomena, (ii) eroded sediment
 166 should be deposited across of the shoal margin, unless eroded sediment deposited in a location
 167 with a high transport capacity, e.g., main channel. Small collapses were not detected because of
 168 the resolution of the bathymetry data (20 m x 20 m), and the date of collapse corresponded to
 169 the bathymetry data in which the collapse was observed, i.e., the collapse occurred in the year
 170 before. VBA (2016) determined solely the locations of shoal margin collapses for the Eastern
 171 part of the Western Scheldt for the period 2000-2015, and used higher resolution and frequency
 172 multi-beam measurement near the tidal flat of Walsoorden to justify their allocated shoal margin
 173 collapses. An example of a well-studied shoal margin collapse that occurred in 2014 (Van Schaick,
 174 2015; Mastbergen and Schrijvershof, 2016) is given in Figure 1. Despite the ability to validate
 175 the approach by well-known collapses, there remained an uncertainty in the identification of shoal
 176 margin collapses because of rapid shoal margin recovery (a few months generally) relative to the
 177 time interval between bathymetry data collection. For example, because of erosion and sedimen-
 178 tation at the shoal margin collapse of 2014, the original shoal margin collapse was not visible after
 179 a year (Jentink, 2015).

180 Shoal margin collapses were manually digitized by drawing a polygon at the boundary of the
 181 eroded part determined from the DoD. These polygons were used to determine characteristic geo-
 182 metric sizes and volumes of the shoal margin erosion scar. The geometry of the collapse was
 183 described by its eccentricity (ϵ). The ϵ is a measure to determine if the shape is a circular. Specif-
 184 ically, $\epsilon = 0$ for a circle, $0 < \epsilon < 1$ for an ellipse, $\epsilon = 1$ for a parabola, and $\epsilon > 1$ is a hyperbola.
 185 The ϵ can be calculated from the semi-major axis (a) and semi-minor axis (b) of the shoal margin
 186 collapse as follow

$$\epsilon = \frac{\sqrt{(a^2 - b^2)}}{a} \quad (1)$$

187 where $\sqrt{(a^2 - b^2)}$ is also known as the the distance between the center of the polygon (circle)
 188 and each focus (f). The volume was calculated from the difference in bed elevation between two

189 consecutive time-steps. We found that the collapsed volume of the shoal margin collapse can be
190 approximated by a part of an ellipsoid, which has volume

$$V = \frac{4}{3}\pi abc \quad (2)$$

191 where c is the third semi-axis and is in this study taken equal to the maximum observed depth of
192 the shoal margin collapse.

193 **3.2 Estuary shape and shoal margin collapses**

194 To understand the location of shoal margin collapses, we related the shoal margin collapse to the
195 following shoal properties. Leuven et al. (Subm) showed that the summed width of shoals (W_b),
196 i.e., bars, approximates the excess width (W_e) as measured in the along-channel direction for the
197 Western Scheldt. Here, the excess width was defined by the active channel width minus the width
198 of the ideal exponential fit, i.e., trumpet shape of the estuary (Savenije, 2015), and the summed
199 width of shoals was defined as the sum of all shoal widths in the cross-section (Leuven et al.,
200 Subm). W_e as well as W_b were determined by the same method as Leuven et al. (Subm). Intuitively,
201 this method showed and predicts bars to fill up that part of the estuary cross-section that is not part
202 of the minimum channel width associated to the ideal estuary. Firstly, a centerline was defined
203 as the mean location line between the polygon boundaries of the Western Scheldt. Secondly, the
204 centerline was smoothed and re-sampled at an interval of 200 m. At all re-sampled points, a cross-
205 section was constructed with a 20 m transverse grid spacing, perpendicular to the centerline and
206 within the boundaries of the Western Scheldt. Finally, the width along the centerline of the estuary
207 was given by the length of the successive cross-sections (Figure 3A). The W_b was calculated by
208 extracting bathymetric profiles at the cross-sections and median depth was determined for each
209 cross-section (Figure 3B). Subsequently, a linear regression was fitted to median depth along the
210 estuary channel, as the estuary depth profile often shows a linear or almost linear profile (Savenije,
211 2015) and the Western Scheldt is no exception. Elevation above the regression line was determined
212 as shoal and W_b was determined as the total width of the bed above this regression line (Figure 3C).

213 We hypothesized shoal margin collapses occur at locations where the summed width of shoals

214 exceeds the excess width, i.e.,

$$\frac{W_b - W_e}{W_e} > 0. \quad (3)$$

215 In case equation 3 is true there are two options: (i) the channel will be pushed by the shoal to
216 migrate laterally (Eke et al., 2014; Van de Lageweg et al., 2014), or (ii) alternatively, in case of
217 a cohesive or protected bank, the channel will deepen (Kleinhans, 2010). Where the Western
218 Scheldt was protected by embankments the channel will deepen and shoal will accrete vertically
219 which would oversteepen the shoal margin, which will increase the transverse slope and may make
220 the shoal margin susceptible to collapses.

221 3.3 Forecasting method to determine the probability of shoal margin collapses

222 Shoal margin collapses in submerged slopes in non-lithified sand and silt-sized sediments form a
223 major threat for flood defenses along estuaries and riverbanks in the Netherlands (Van den Ham
224 et al., 2014). Therefore, bank safety assessments were developed for assessing dike failure prob-
225 ability by flow-sliding. Van den Ham et al. (2014) proposed a practical, semi-empirical method
226 for assessing flow-sliding on a transverse profile at the shoal margin, which results in a probabilit-
227 ity per km per year that was representative for a (uniform) slope section with a certain length.
228 This method was based on statistical information about the documented historical flow slides
229 of Wilderom (1979) per km of channel banks, in which the results of complex theoretical mod-
230 els, describing physics of static liquefaction or breach-flow, were incorporated. The database of
231 Wilderom (1979) mainly included flow slides at channel banks for obvious reasons of dike safety,
232 but we assumed that the processes for flow slides on the shoals were the same and that this bank
233 safety assessment of WBI (2017) could be applicable as a forecasting method for the less steep
234 shoal margins as well.

235 The basic equation for the bank safety calculates the frequency for a liquefaction flow-slide and
236 breach flow-slide:

$$F(SC_{liquefaction}) = \left(\frac{H_R}{24}\right)^{2.5} \cdot \left(\frac{5}{cot\alpha_R}\right)^5 \cdot \left(\frac{1}{10}\right)^{-10(0.05+\psi)} \cdot \frac{V_{local}}{V_{WS}} \cdot \frac{SC_{avg}}{L_{sm}} km/year \quad (4)$$

237 and

$$F(SC_{breach}) = \left(\frac{H_C}{24}\right)^5 \cdot \left(\frac{5}{\cot \alpha_R}\right)^5 \cdot \left(\frac{2 \cdot 10^{-4}}{D_{50}}\right)^5 \cdot Fr_{clay} \cdot \frac{V_{local}}{V_{WS}} \cdot \frac{SC_{avg}}{L_{sm}} km/year \quad (5)$$

238 where H_R and α_R are the relative height and angle for a fictitious slope. V_{local} is the local bank
239 migration rate and V_{WS} is the average bank migration in the Western Scheldt (1 m/yr). ψ is the
240 state parameter as a function of a cone penetration test (CPT) according to relation by Shuttle and
241 Jefferies (1998), which is the average value of the state parameter in the soil layers between top
242 and toe of the submerged slope, with a (cumulative) thickness of 5 m having the loosest packing
243 (highest state parameter). A negative ψ indicates dense, dilative soils, whereas a positive ψ in-
244 dicates loose contractive soils (see also Van Duinen et al., 2014). SC_{avg} is the average number of
245 collapses a year and L_{sm} is the total length of the shoal margins based on our documented shoal
246 margin collapses. D_{50} is the averaged grain-size over all sand layers between top and toe of the
247 submerged slope. Fr_{clay} is factor for the clay-layers, where Fr_{clay} is 1/3 for absence of clay layers
248 and Fr_{clay} is 3 for many clay layers.

249 The triggering of liquefaction is strongly determined by the effective stress conditions in the
250 saturated sand. These are determined by the steepness, height of the slope and the level of the
251 phreatic line: soil above the phreatic line has a higher weight than the submerged weight. In
252 order to enable comparison between completely submerged slopes and slopes that are partly above
253 the water level (phreatic line below surface level), Van den Ham et al. (2014) introduced a so-
254 called fictitious slope (H_R and α_R) (Figure 4A), as if the complete slope is submerged. So at low
255 water level (LWL) the fictitious slope is higher than at high water level (HWL), indicating that
256 the probability on slope collapse is the largest at LWL. For this study this is less relevant since
257 the majority of the slopes will be almost completely submerged. For that reason here we used for
258 breaching and liquefaction the same height (so $H_R = H_C$) that is completely submerged (Figure 4A).

259 In this study, we modified the calculation of H_R to make it applicable to spatial bathymetry data.
260 H_R was determined for each grid cell by determining the maximum height difference (Δh_{max}) from
261 the center to the deeper part within a window. Here, H_R was in the range of H_C as this only takes
262 account of the height difference between two points instead of adding a fictitious slope geometry
263 that contributes to the stress. The α_R was calculated as the angle between the cells with Δh_{max} and

264 their distance (ΔL , Figure 4B). For the window size we used the median size of the shoal margin
 265 collapses (A_{50}), but we also tested the sensitivity of the window size on the probability values.

266 The form of the above relation allows frequency to be higher than 1, which was prevented by a
 267 transformation, namely a Poisson process, of the frequency into a probability ($P(FS)$):

$$P(SC) = 1 - e^{-F(SC)} \quad (6)$$

268 The bathymetry data enables quantification of the spatial variation in H_R and α_R for equations 4
 269 and 5. Because of the lack in spatial information and the distribution for the variables D_{50} , ψ and
 270 Fr_{clay} , fixed values were considered corresponding to the average values for the Western Scheldt
 271 of $2 \cdot 10^{-4}$, -0.05 and 1, respectively. Since information was lacking about the type of flow slides,
 272 the assumption was made that half of all flow slides were pure liquefaction flow slides while the
 273 other half concerned pure breach flow-slides (Van den Ham et al., 2014; Van Duinen et al., 2014),
 274 i.e.,

$$P(SC) = 0.5P(SC_{breach}) + 0.5P(SC_{liquefaction}) \quad (7)$$

275 Initially we excluded the spatial variation in Fr_{clay} and ψ and applied a constant value because
 276 of the lack of spatial information. Later, we extended the shoal margin collapse predictor to in-
 277 clude a spatial variable Fr_{clay} (equation 5) and ψ (equation 4) because these variables might affect
 278 the predicted shoal margin collapse locations. However, as spatial data for these variables were
 279 unavailable some assumptions had to be made for a tentative test. The first assumption was that
 280 information about the spatial distribution of clay probability could give an indication for spatial
 281 variation in clay layers. We assumed that the distribution of clay has not changed significantly
 282 over the past within the shoals and that clay fraction measured at the surface is a first-order esti-
 283 mate for the amount of clay layers within the submerged slope, for lack of more information. We
 284 used the dataset from the GeoTOP model of TNO (2016), which provided information about the
 285 probability that the lithological unit clay was found within a grid cell of 100 x 100 m for the top
 286 50 cm (also see Braat et al., 2017). A value for Fr_{clay} was assigned based on the probability of clay
 287 for TNO (2016) data, where $Fr_{clay} = 1/3$ for less than the median, $Fr_{clay} = 1$ for locations equal to

288 the median, and $Fr_{clay} = 3$ for locations with more than the median.

289 The second assumption was that the age of the deposits determines the state parameter, ψ . We
290 assumed that aged sands were more resistance with time because of consolidation (Biot, 1941) due
291 to cementation and compressibility, and that ψ increased lognormal for the saturated sediments
292 with the age of the deposit (Hayati and Andrus, 2009). ψ was determined by the subsurface
293 of the submerged slopes. In earlier work, the subsurface was described by three stratigraphic
294 units (Wilderom, 1979): i) Jong zeezand, 2) Oud zeezand, and 3) Pleistocene sand. Both Jong
295 zeezand and Oud zeezand concern tidal deposits, although from different age, and was deposited
296 very quickly, resulting in very low densities. The estimated average ψ varies for these various
297 stratigraphic units from 0, -0.05 and -0.1 for Jong zeezand, Oud zeezand and Pleistocene sand,
298 respectively. A ψ was assumed based on the age of the deposits for the top 5 m, where the oldest
299 deposits (deposited in 1959) had a ψ value of -0.05 and the youngest deposits (deposited in 2015)
300 had a ψ value of 0. A lognormal function, i.e., $\psi_T = -0.0125 \log (2015-T)$ with T is year of
301 deposit, was applied between the youngest and oldest sediments to determine a state parameter
302 for sediment ages (ψ_T), which was then multiplied by its fraction (f_T) within the top 5 m of the
303 deposits. The spatial variable state parameter (Ψ_{T5}) follows as

$$\Psi_{T5} = \sum_{T=1}^{55} f_T \psi_T \quad (8)$$

304 where T is year of the sediment deposition with $T=0$ for 1959. f_T is the fraction of deposited
305 sediment for year T in the top 5 m.

306 Finally in the discussion, we performed a multi-regression analysis on the various variables
307 and test if the forecasting method for shoal margin collapses can be improved. Additionally, a
308 multi-regression analysis is performed on the variables to determine the shoal margin collapse size
309 and volumes. In the discussion, we also provided several equations for determining the geometric
310 dimension, i.e., the axis abc , of the shoal margin collapses, which can be included in a numerical
311 morphodynamic model.

312 **3.4 Validation of the forecasting method by receiver operating characteristics**

313 The forecasting method returned a probability map of shoal margin collapses for the Western
314 Scheldt. To quantitatively compare these probability maps with binary values of [0,1] for locations
315 without or with shoal margin collapse, we calculated a receiver operating characteristic (ROC)
316 curve. This curve indicates the performance of a binary classifier system (in this case, shoal margin
317 collapses) as the probability threshold $P(SC)$ is varied (see also Van Dijk et al., 2016). The curve
318 was constructed by plotting the true positive rate (TPR), defined as the number of cells that had
319 shoal margin collapses in both the predictive probability and observed collapses divided by the
320 number of observed locations of collapses, against the false positive rate (FPR), defined as the
321 number of cells that had shoal margin collapses in the predictive probability but no observations of
322 collapses divided by the number of cells with no shoal margin collapse observations. The TPR and
323 FPR were calculated for various threshold values of $P(SC)$. Increasing the threshold for $P(SC)$
324 led to fewer cells being classified as locations of shoal margin collapses, and should lead to a
325 decrease in both TPR and FPR. ROC curves were constructed for various window sizes, and for
326 the shoal margin collapses prediction that includes the spatial variation of clay or relative density.
327 An effective model should show a higher TPR at a given FPR than random prediction, which was
328 summarized by the area under the ROC curve (AUC).

$$AUC = \int_{-\infty}^{\infty} TPR(D)FPR(D)dT \quad (9)$$

329 where D is the given threshold parameter, and assumed is that the positive ranks higher than nega-
330 tive. The AUC measures discrimination, that is, the ability of the test to correctly classify location
331 with and without shoal margin collapses. The area under the curve is the percentage of randomly
332 drawn pairs for which the test correctly predicts the shoal margin locations. A random predictor
333 will give an AUC of 0.5, whereas an excellent predictor will give an AUC of 0.9-1.0.

4 Results

4.1 shoal margin collapses

Analysis of consecutive bathymetry data enable us to distinguish a total of 299 shoal margin collapses in the period 1959-2015 (Figures 2A, 5A). This means that on average 5.3 collapses (SC_{avg}) occur per year in the Western Scheldt. The 299 shoal margin collapses that are identified included mainly collapses at the shoal margins and only a few at the channel banks. From the fitted regression line for the median depth along the estuary, shoal margins were distinguished and the migration of the shoals were tracked in the Western Scheldt (Figure 2B). The total measured shoal margin length (L_{sm}), excluding the channel banks, is 300 km for the Western Scheldt. The size of the collapses varies from about 3,000 m² to 300,000 m² with a median size of 34,000 m² (Figure 5B). The shoal margin collapse sizes are log-normal distributed with a mean μ of 10.38 and a standard deviation σ of 0.88 with a skewness of 2.26. The volume of the collapses varies from 6,000 m³ to 3,000,000 m³ with a median volume of 100,000 m³. The shoal margin collapse volume is also log-normal distributed with a mean μ of 11.59 and a standard deviation σ of 1.21 with a skewness of 3.56.

The shape of the shoal margin collapses is described by the three semi-axes abc . In general, the semi-axis a and b are not equal (Figure 6A). Analysis of both lengths show that even for the longest and widest collapses axis c , i.e., the thickness, does not scale with the size of the collapse. The eccentricity (ϵ) indicates that the planform shape of collapses are not circles ($\epsilon = 0$) but more likely have a shape of an ellipse with ϵ mostly between 0.8 and 1 (Figure 6B), where an ϵ of 1 indicates a parabola shape. The volume of the shoal margin collapses are best predicted by 1/3 of an ellipsoid, probably because of the slope at the shoal margin (see Figure 6C).

Sediment deposition volume mirrors the sediment erosion volume over time and both vary along the Western Scheldt. The total eroded sediment volume is more or less the same as the total accreted sediment volume (Figure 7A). A high volume of sediment erosion is visible around the tidal flat Hooe Platen (g in Figure 2A) near the estuary mouth, and between Terneuzen and the tidal flats of Ossensisse (d in Figure 2A). Shoal margin collapses occur along the full length of

361 the Western Scheldt (Figure 7A), but several peaks in the eroded volume correspond to locations
362 with multiple shoal margin collapses, indicating a local disturbance of sediment input. However,
363 the volume of the shoal margin collapses are relative small compared to the total eroded sediment
364 volume for the period 1959-2015. Furthermore, the peak of eroded sediment volume between km
365 21 and km 26 (Terneuzen and the tidal flats of Ossensisse) does not correspond with a peak in the
366 number of shoal margin collapses. In conclusion, over the period 1959-2015 only 2% of the total
367 eroded sediment volume is made up by the volume of the shoal margin collapses (Figure 7B).

368 We hypothesized that the location of the shoal margin collapses could relate to a normalized
369 W_b . Analysis of the shoal margin collapses along the Western Scheldt suggests that for $(W_b -$
370 $W_e)/W_e > 0$, the margin is susceptible to collapses (Figure 8A). However, there is no relation
371 between the number of collapses at a cross-section and the value for $(W_b - W_e)/W_e$ along the
372 Western Scheldt (Figure 8B). Even in some cross-section $(W_b - W_e)/W_e$ is larger than 0, but no
373 shoal margin collapses occurred. Particularly, between Terneuzen and the tidal flats of Ossensisse
374 around 25 km from the mouth no shoal margin collapses occurred, even with a $(W_b - W_e)/W_e$ of
375 0.5. This corresponds to the same location where the volume of sediment erosion and deposition is
376 relatively high (Figure 7A). Analysis of the variation in the summed width of shoals, as indicator
377 for the migration rate, shows that the variation is not significantly higher for locations with shoal
378 margin collapses (Figure 8C). Therefore, for the forecasting method of the shoal margin collapses
379 we excluded the factor V_{local}/V_{WS} in equations 4-5 and suggest that lateral migration rate is instead
380 relative low for locations with shoal margin collapses as collapses reoccur at the same location.

381 **4.2 Shoal margin collapse assessment**

382 **4.2.1 The probability of shoal margin collapses**

383 From the bathymetry data the relative slope height and angle are calculated, which are applied
384 in the forecasting method to determine the probability of shoal margin collapses. In the initial
385 calculations a constant value was taken for ψ and Fr_{clay} of -0.05 and 1, respectively, that represents
386 the mean in the Western Scheldt. SC_{avg} and L_{sm} of 5.3 and 300 km, respectively, are calculated
387 for the Western Scheldt, whereas the variables V_{local} and V_{WS} are excluded from the forecasting

388 method (see previous section). Because of the spatial information of the bathymetry a spatial
389 probability map is generated that predicts the probability of a shoal margin collapse in the Western
390 Scheldt.

391 Figure 9A shows the variation in the relative slope height for the Western Scheldt in 2015. The
392 shoal margins and channel banks have a typical value of $H_R > 1$, while the channels and shoals
393 itself have a value of less than 1 m. The histogram of the probability illustrates that most values are
394 less than 5 m for the Western Scheldt and the shoal margins, but that for the locations with shoal
395 margin collapses it is more likely to have a H_R of more than 5 m (Figure 9B). The median height
396 ($H_{R,50}$) for the shoal margin collapses is 11 m. The spatial map of α_R (Figure 9C) shows that a
397 major part of the Western Scheldt has an $\alpha_R < 1^\circ$, i.e., $\cot(\alpha_R) = 45$ (Figure 9D), and a steeper α_R
398 corresponds to higher H_R values. The histogram of the probability illustrates that most slopes are
399 steeper than 3° , i.e., $\cot(\alpha_R) = 19$, for the shoal margin collapses, whereas the general slope of the
400 shoal margins is less than 3° .

401 H_R and α_R combined in the shoal margin collapse predictor shows spatial variation in the prob-
402 ability along the shoal margins (Figure 9E). Bank protection measures on the northern but mainly
403 southern banks of the Western Scheldt correspond to location with high probabilities, and therefore
404 the analysis focuses mainly on the shoal margins. Also high probabilities are found at the edge of
405 the shallower part between Vlissingen and Borsello (so called Honte). Migration of the deeper part
406 (below -24 m NAP) in the Honte of the Western Scheldt was slower than the shallower part (above
407 -24 m NAP = Amsterdam Ordnance Datum), which led to the development of a plateau at a depth
408 of -24 m NAP. This plateau is insusceptible to shoal margin collapses, because of the resistant
409 layer formed by shell deposits (so called 'craggs', Cleveringa, 2013). Calculation of the probability
410 shows different outcomes for shoal margin collapses by breaching and liquefaction (Figure 9F). In
411 general, the probabilities for breaching are lower compared to liquefaction. As the type of flow
412 slide is unknown a combined probability (equation 7) gives probability values (almost) comparable
413 to probabilities for liquefaction. Variation in the window sizes shows that with a larger window
414 size (300 x 300 m) than the average collapse size (A_{50}) the probabilities increases slightly, mainly
415 because of the increase in H_R , whereas α_R decreased (Figure 9F).

416 4.2.2 Role of spatial variation of clay-layers and state parameter on the assessment

417 In the initial calculation for the probability we assumed a constant value for FR_{clay} and ψ , whereas
418 it is more likely that these spatially vary as well. The GeoTOP model of clay probability is used to
419 assess if the spatial variation of clay associated to clay-layers improves the prediction of the shoal
420 margin collapse locations. The spatial distribution of clay probability from the GeoTOP model
421 (Figure 10A) shows that for most locations with shoal margin collapses the clay probability is
422 higher than the average probability (Figure 10B).

423 The bathymetry data is used to estimate a spatial distribution of state parameter (Ψ_{T5}) based on
424 the relative age. From consecutive bathymetry data is noticed that the relative age of the surface
425 is actually young for most tidal flats/ shoals (Figure 10C). This is also true for the ages of the
426 collapsed shoal margin sediments. Most eroded sediment has been reworked within 10 years
427 (Figure 10D), which is determined by the age difference between two consecutive age of surface
428 maps. The Ψ_{T5} value is determined by the age of the top 5 m of the deposits, and shows relative
429 high values at the shoal margin and in the secondary channels that are slowly filling up for 2015
430 (Figure 10E). The proposed Ψ_{T5} identifies large areas with a Ψ_{T5} closer to -0.05, i.e., deposited in
431 1959, whereas the locations with shoal margin collapses have generally a Ψ_{T5} value higher than
432 -0.05, i.e., closer to deposits from 2015 (Figure 10F). In general, this indicates that shoal margin
433 collapses mainly occur at locations with young 'loosely packed' deposits. Because the age of the
434 deposits that were eroded is younger than 10 years, we argue that the generated Ψ_{T5} map of 2015
435 could be used to determine a ψ value for the forecasting method. Generated Ψ_{T5} maps for each
436 single time step shows that about 30% of the collapses occurred on the initial bathymetry of 1959.
437 However, as there is no actual age of deposition for sediments deposited before 1959, we decided
438 to exclude these locations from the probability distribution of Ψ_{T5} . Without these locations the
439 distribution is more comparable to the distribution for collapses based on the 2015 Ψ_{T5} map than
440 the overall distribution of Ψ_{T5} for the Western Scheldt (Figure 10H).

441 4.2.3 Accuracy of the probability of shoal margin collapses

442 The ROC curves allow us to examine the probability of shoal margin collapses and the effect of
443 a threshold on the accuracy between the predicted locations and the actual shoal margin collapse
444 locations. The ROC curve probabilities are calculated only for the shoal margins, because the
445 forecasting method showed that high chances for collapses also occur for the channel banks, but
446 these parts are protected from collapses and thus would result in a higher false positive rate (FPR).
447 In the case of random prediction, increasing the threshold (that is, increasing the probability value
448 needed to assign shoal margin collapses in the final map) causes a proportionate decrease in both
449 TPR and FPR. This is represented by the straight line in Figure 11. Overall, the shoal margin
450 forecasting method performs better for increasing threshold values, as shown by the increasing
451 ratio of TPR to FPR (Figure 11A). The range in Figure 11A represents the outcomes from using
452 bathymetry data of different years with a map of shoal margin collapse occurrences. Although the
453 probabilities were lower for a window size of 300 m, the ratio of TPR to FPR is higher, meaning
454 that a large window is better in predicting a spatial variation that translates into more accurate
455 prediction of the shoal margin collapse locations. The area under the ROC curve (AUC) varies
456 from around 0.7 for the older bathymetry data to 0.8 for the bathymetry data of the last decade,
457 meaning that the increased precision of the bathymetry data predictions become more accurate.
458 A probability threshold of about 10^{-7} is sufficient to predict at least half of the shoal margin
459 collapse locations, while FPR remains low. Keep in mind that because only 7% of the shoal
460 margin collapsed and not 50%, at the threshold of 10^{-7} the FPR is lower than the TPR but in
461 absolute numbers more locations are falsely identified as a shoal margin collapse.

462 Including spatial variation of clay or the relative age did not increase the quality of the predic-
463 tion. We suspect that the inclusion of Fr_{clay} based on the GeoTOP model would not affect the
464 prediction of the shoal margin collapse locations as there is significantly no change between the
465 distribution of the shoal margin collapses and other locations of the Western Scheldt (Figure 10B).
466 The GeoTOP data, with an equal distribution (Figure 10B), shows no change in the prediction
467 according to the ROC curve (Figure 11B). This implies that the current clay probability maps
468 are not sufficient in predicting the spatial variation in clay-layers or that the role of clay-layers

469 in the occurrence of shoal margin collapses could be neglected. Including a spatial Ψ_{T5} , which
470 distribution does differ between the shoal margin collapse location and the Western Scheldt (Fig-
471 ure 10E), shows not a significant change in the improvement of the prediction in the ROC curve
472 (Figure 11B). This suggest that although a spatial variable Ψ_{T5} , its role on predicting shoal margin
473 collapses is insignificant in the current equation 4, and that the probability is mainly determined
474 by the variation in H_R and α_R .

475 **5 Discussion**

476 This study characterized the spatial distribution and geometries of shoal margin collapses in the
477 Western Scheldt for 1959-2015 and tested a spatial forecasting method on the basis of bathymetric
478 data. Below, we discuss our observations in comparison to an earlier study of Wilderom (1979).
479 We also propose modification of the forecasting method based on our observations and compare the
480 accuracy with the tested forecasting method. Finally, we consider the implication of the forecasting
481 method for numerical modeling.

482 **5.1 Comparison with Wilderom (1972)**

483 The present study of shoal margin collapses in the Western Scheldt, based on digitized bathymetry
484 data from 1959 to 2015, actually provides an update of the database of Wilderom (1979), enabling
485 us to update statistical data on location, geometry and occurrence intervals of this type of bank
486 collapses (flow slides). It is surprising that such a large number of shoal margin collapses could
487 be detected from the data, since it was hardly publicly known or observed. Because the process
488 remains completely under water in general. Also, large collapses were detected in the Eastern
489 Scheldt bathymetry data but remained unnoticed for years (De Groot and Mastbergen, 2006). The
490 large shoal margin collapse at the tidal flat of Walsoorden in 2014, however, created a large erosion
491 scar above the low water level of the shoal and generated therefore a lot of public attention.

492 Our analysis of shoal margin collapses overlaps with the observations of Wilderom (1972) for
493 the period 1959-1972. Wilderom (1972) describes shoal margin collapses at several tidal flats in the
494 Western Scheldt (see Figure 2A); the Spijkerplaat west (a) and east (b), tidal flat of Walsoorden (c),

495 tidal flats of Ossenisse (d), Middelpmaat (e), and Brouwersmaat (f). Our study indicates that besides
496 these tidal flats also shoal margin collapse occur at the tidal flat of Hooge Plaat (g) and at the
497 tidal flats north of the Verdrongen Land van Saefinghe (h). We were not able to identify all shoal
498 margin collapse of Wilderom (1972) that were specifically mentioned. For example, the collapse
499 of 1964 of 3.5 million m³ at the eastern part of the Spijkermaat was not detected as we missed
500 bathymetry for this part of the Western Scheldt for 1965. We also argue that the volumes that
501 we observed are conservative and likely underestimated, because of the yearly intervals between
502 subsequent bathymetries can cause reworking and infilling of the collapse.

503 Our interpretation of the bathymetry indicates changes in shoal margin collapses for the several
504 tidal flats compared to the observations of Wilderom (1972). At the Spijkermaat no major collapses
505 occur at the east side after 1970, while the west side of the Spijkermaat remains very active with
506 collapses in the three years. The western part of tidal flat of Walsoorden that was subjugated to
507 erosion according Wilderom (1972) became less active after shortening of the groyne near the town
508 of Walsoorden, but the southern part of the tidal flat became susceptible to shoal margin collapses
509 in the last decade, showing several large shoal margin collapses (Van Schaick, 2015). The tidal flats
510 of Ossenisse have the most shoal margin collapses over time; in correspondence with Wilderom
511 (1972). The shoal margin collapses at the Middelpmaat, however, are less clearly defined from the
512 bathymetry and the specific collapses of Wilderom (1972) are not detected, probably because of
513 general deepening of the channel the conditions do not follow our criteria (see method section).
514 Also the specific collapse at the Brouwersmaat is not detected, although we do observe several
515 shoal margin collapses after 1970. In general, the the locations for shoal margin collapses reported
516 by Wilderom (1972) and this study coincide with the higher probabilities from the forecasting
517 method.

518 **5.2 Forecasting method to determine the probability of shoal margin collapses**

519 The current forecasting method provides a tool to estimate the probability of expected collapses at
520 banks and shoals. The current analysis indicates that the variables relative height (H_R) and angle
521 (α_R) are the major contributors for the frequency as well as the probability value. The current

522 predicted frequency for shoal margin collapses is low, because H_R is divided by 24, which is based
523 on the average height for channel bank collapses in the Western Scheldt. But also the variable α_R
524 is based on an average value of $\cot\alpha_R$ of 5. However, our analysis for the shoal margin collapses
525 shows an average height of 11 m (H_R) and an average slope of 6° (α_R , i.e., $\cot\alpha_R$ of 9.5). Changing
526 the values 24 and 5 into 11 and 9.5, respectively, will increase the predicted frequency but not
527 accuracy of the predicted locations. Our findings suggest that the proposed Ψ_{T5} , based on age of
528 deposition, for the shoal margin collapse locations is different than the constant ψ used for the
529 Western Scheldt, and could improve the predicted. However, in the current forecasting method the
530 power of ψ on the frequency is not significant. A multiple regression analysis shows that there is
531 not much correlation between the three variables and the frequency of collapses, as also suggested
532 by Van den Ham et al. (2014) for the historical data of Wilderom (1979).

533 Our findings do indicate that the distribution of ψ varies for the locations with collapses com-
534 pared to Western Scheldt. Introducing a stronger factor for ψ in the forecasting method did show
535 a shift in the ROC curve, with increasing TPR over FPR for higher threshold values but the AUC
536 remains the same as for lower threshold values TPR over FPR decreases. These findings indicate
537 that the forecasting method could be improved in the future by adjusting the variable of ψ , but this
538 mainly improves the prediction for the observed locations with multiple collapses, and therefore
539 consist of younger less consolidated sediments. These multiple collapses occur at immobile tidal
540 shoals that have a high and steep boundary, but are dynamic in vertical direction due to erosion and
541 accretion, whereas horizontally dynamic shoals, due to channel migration, which is included in the
542 original equations 4-5 of Van den Ham et al. (2014), are not susceptible to collapse. Including a
543 ψ value based on age would work for the shoal margin in the Western Scheldt, where continuous
544 new deposition increases the tidal flat levels, whereas in the Eastern Scheldt the elevation of the
545 tidal flats decreases (De Vet et al., 2017).

546 Analysis of the geometric shape of the erosion scar from the shoal margin collapses does not
547 show a direct relation between the area size or volume with one of the variables, i.e., H_R , α_R , ψ or
548 Fr_{clay} . According to a multi-regression analysis the collapsed size and volume is mostly affected
549 by α_R , Fr_{clay} , and ψ . Earlier analysis of Silvis and De Groot (1995), however, predicted the length

550 of the erosion scar by the slope of the shoal but mainly the channel depth. The model D-Flow Slide
551 (WBI, 2017), based on the findings of Silvis and De Groot (1995), calculates the probability on a
552 retrogression length of the erosion scar, which is a function of a number of geometric parameters
553 before collapse and a volume balance between the material eroded from the scar and deposited at
554 the toe. This method mainly predicts a larger retrogression length for a higher H_R , but according
555 to our multi-regression analysis there is no relation between H_R and the geometric shape.

556 **5.3 Potential use of the forecasting method**

557 The probability on bank collapses is a well-studied problem as many collapses either threatened
558 or destroyed dikes and led to flooding. The additional data of shoal margin collapses from this
559 study combined with the historical database of (Wilderom, 1979) gives insights in the conditions
560 under which collapses occur. Current bank assessments in the Netherlands are conducted on cross-
561 sections represent a stretch of the bank (WBI, 2017) and probabilities are tested for observed bank
562 collapse locations (Stoutjesdijk et al., 2012). This study proves that the forecasting method for
563 determination of shoal margin collapses is also applicable on spatial data, and even for interpolated
564 elevation data on a fixed Cartesian 20x20 m grid. Although the calculated frequency are evidently
565 lower than observed there remains a spatial variation in the probability that collapses do occur in
566 the Western Scheldt.

567 The forecasting method is designed to be generic and could be applied for other estuaries as
568 well. Although shoal margin collapses are not reported for many other estuaries, analysis on
569 bathymetry data of the Dovey and Mersey estuaries (see also Leuven et al., Subm) shows that the
570 relative slope angles and height are less than for the Western Scheldt (Figure 12). Bathymetry data
571 of the Lower Columbia Estuary from 2009-2010 (LCEP, 2010), however, has comparable slopes
572 as the Western Scheldt (Figure 12) but no shoal margin collapses are reported in the literature. The
573 steeper margins of the Lower Columbia Estuary exist of vegetated wetlands (Marcoe and Pilson,
574 2013), which strengthen the shoal margin for sudden collapses. The unvegetated tidal flats are,
575 however, lower and therefore less susceptible to flow slides. The steeper and higher slopes in the
576 Lower Columbia could, like the Western Scheldt, be associated to dredging activities, as a fairway

577 is maintained towards Portland (Willingham, 1983; Cannon, 2015). Some of the lower unvegetated
 578 tidal flats are designated for the disposal of maintenance dredging material, e.g., at Rice Island and
 579 Miller Sands (Cannon, 2015). This could cause a flow side, if the dumped material flows over the
 580 submerged slope, initiating an eroding turbulent density current, but would also lead to an increase
 581 in slope steepness and height.

582 Morphodynamic models show a tendency to overdeepen channels with the current transverse
 583 slope predictors (Van der Wegen and Roelvink, 2012). Overestimating the transverse slope effect
 584 in the morphodynamic model, and thus more downslope sediment transport, may be necessary to
 585 flatten the morphology and compensate for subgrid bank erosion processes that usually does not
 586 occur in the numerical models (Grenfell, 2012; Schuurman et al., 2013; Van Dijk et al., 2014). Baar
 587 et al. (Subm), however, concluded that overdeepening is not a direct result of the current transverse
 588 bed slope predictors. We propose to implement the forecasting method into a numerical morpho-
 589 dynamic model such as Braat et al. (2017) to oppose the transverse bed slope effect that steepens
 590 the shoal margin slope. Including the process of shoal margin collapses into a morphodynamic
 591 model might reduce the tendency to overdeepen the channels without having to overestimate the
 592 transverse bed slope predictor. The first step towards implementation of shoal margin collapses
 593 could be to replace the existing (overly simplistic) bank erosion forecasting method with the modi-
 594 fied forecasting method, which collapses all slopes above a critical probability to a post-event slope
 595 whilst conserving mass. The geometric shape of the erosion scar, i.e., the semi-axis abc , could be
 596 calculated for a given eccentricity, shoal margin collapse size, and the volume for a geometric
 597 shape of 1/3 ellipsoid as follow

$$a = \frac{\sqrt{A_{collapse}}}{\sqrt{\pi} \cdot \sqrt[4]{1 - \epsilon^2}} \quad (10)$$

$$b = \sqrt{a^2 - \epsilon^2 \cdot a^2} \quad (11)$$

$$c = \frac{3 \cdot V_{collapse}}{\frac{4}{3} \pi ab} \quad (12)$$

598 where ε varies between 0.75 and 1. There is no direct relation between the variables (H_R and
599 α_R) and area size and volume. Therefore, we suggest that $A_{collapse}$ and $V_{collapse}$ should be
600 randomly picked from the observed log-normal distribution, where for $A_{collapse}$ the distribution is
601 created with a μ of 10.38 and a standard deviation σ of 0.88 and for $V_{collapse}$ the distribution is
602 created with a μ of 11.59 and a standard deviation σ of 1.21, according to the 299 observed shoal
603 margin collapses between 1959-2015.

604 A scientific application of our spatial shoal margin collapse forecasting method will be to test
605 the role of perturbations of the deposited collapsed material in the main channel of tidal systems. In
606 tidal systems perturbations likely propagate in both directions depending on channel ebb or flood
607 dominance, but how far and how fast has not been studied. Connections to the rest of the network
608 may also determine whether perturbations excite or dampen. Conceptually, the downstream water
609 and sediment fluxes, flow momentum and curvature, and upstream-propagating backwater effects
610 (Friedrichs and Aubrey, 1988) can be seen as propagation of a signal or perturbation. We hy-
611 pothesize that such morphological perturbations within the system may dynamicise the presently
612 underpredicted morphodynamics of estuaries as much as extreme events in the boundary condi-
613 tions.

614 **6 Conclusions**

615 We studied the dimensions, geometry and probability of shoal margin collapses in the Western
616 Scheldt for the period 1959-2015 and determined characteristic locations on various tidal flats that
617 are susceptible to shoal margin collapse. Shoal margin collapses occur at immobile tidal shoals that
618 have a high and steep boundary, but are dynamic in vertical direction due to erosion and accretion,
619 whereas horizontally dynamic shoals, due to channel migration, are not susceptible to collapse.

620 We tested a modified algorithm that for the first time is applied on bathymetry data to assess
621 the probability of shoal margin collapses, which showed that the probability of shoal margin col-
622 lapses spatially varies but the frequency for a collapse are on average lower than observed. The
623 spatial variation in the probability is, however, sufficient to predict shoal margin collapse locations
624 according to the receiver-operating characteristic curve. In future studies we now can implement

625 the forecasting method and apply a realistic geometric shape of shoal margin collapse, and study
626 the role of shoal margin collapses on the long-term development of estuaries. Nevertheless, the
627 forecasting method could be further improved for locations with multiple shoal margin collapses
628 by including a higher factor for the spatial variable state parameter, which is until now to be con-
629 sidered as a constant value for the Western Scheldt.

630 Specifically our results show that:

- 631 • Tidal shoals are mainly found where the estuary width exceeds the ideal trumpet shape.
- 632 • Shoal margin collapses occur at locations where the summed width of shoals exceeds the excess
633 width. When the channel banks are fixed or protected these shoals are laterally inactive and shoal
634 margin collapses occur as these shoals are vertical dynamic, i.e., steepening of the slope followed
635 by flow slides.
- 636 • Shoal margin collapses cover on average an area of 34,000 m² and a volume of 100,000 m³ with
637 volumes up to more than 1,000,000 m³, and contribute about 2% of the total erosion in the Western
638 Scheldt.
- 639 • The geometric shape of the shoal margin collapse can be simplified by 1/3 of an ellipsoid for the
640 purposes of modelling.
- 641 • Slope height and angle are good indicators to predict the locations for shoal margin collapses in
642 the Western Scheldt.
- 643 • Forecasts could be improved when we account for locations that are subjugated to multiple shoal
644 margin collapses by including a variable for the age of the deposit or adapt the variable of the state
645 parameter ψ .

646 **7 ACKNOWLEDGEMENTS**

647 This project was supported by the Netherlands Organisation for Scientific Research (NWO, grant
648 STW-Vici-016.140.316/13710 to MGK for WvD and JL). We gratefully acknowledge Marco Schri-
649 jver (Rijkswaterstaat) and Marcel Taal (Deltares) for insightful discussions. We thank Rijkswater-
650 staat for providing the bathymetry data of the Western Scheldt. Reviewers will be acknowledged.
651 To obtain the data used in this paper, please contact the authors.

References

- 652
- 653 A. W. Baar, J. De Smit, W. S. J. Uijttewaal, and M. G. Kleinhans. Sediment transport of fine sand
654 to fine gravel on transverse bed slopes in rotating annular flume experiments. *Water Resources*
655 *Research*, Subm.
- 656 K. Beinssen, D. T. Neil, and D. R. Mastbergen. Field observations of retrogressive breach failure
657 at the two tidal inlets in Queensland, Australia. *Australian Geomechanics*, 49(3):55–64, 2014.
- 658 M. A. Biot. General theory of three-dimensional consolidation. *Journal of Applied Physics*, 12(2):
659 155–164, 1941.
- 660 L. Braat, T. Van Kessel, J. R. F. W. Leuven, and M. G. Kleinhans. Effects of mud supply on large-
661 scale estuary morphology and development over centuries to millennia. *Earth Surface Dynamics*
662 *Discussion*, in review, 2017. doi: 10.5194/esurf-2017-14.
- 663 L. Cancino and R. Neves. Hydrodynamic and sediment suspension modelling in estuarine systems.
664 *Journal of Marine Systems*, 22:117–131, 1999. doi: 10.1016/S0924-7963(99)00036-6.
- 665 C. M. Cannon. Landforms along the Lower Columbia River and the influence of humans. Master’s
666 thesis, Portland State University, 2015.
- 667 H. A. Christian, P. A. Monahan, and D. C. Mosher. Initiation of underwater flowslides in a river
668 and tide-dominated system: the Fraser river delta. In *International IAEG Conference*, volume 8,
669 pages 3827–3832. Balkema, Rotterdam, 1998.
- 670 J. Cleveringa. Ontwikkeling mesoschaal Westerschelde - instandhouding vaarpassen Schelde Mi-
671 lieuvergunningen terugstorten baggerspecie (in Dutch). Technical report, ARCADIS, 2013.
- 672 J. M. Coleman. Brahmaputra River: channel processes and sedimentation. *Sedimentary Geology*,
673 3:129–239, 1969. doi: 10.1016/0037-0738(69)90010-4.
- 674 G. Dam, A. J. Bliiek, R. J. Labeur, S. Ides, and Y. Plancke. Long term process based morphological
675 model of the Western Scheldt Estuary. In *Proceeding of the 5th River, Coastal and Estuarine*
676 *Morphodynamics*, pages 1077–1084, Enschede, The Netherlands, 2007. IAHR.

- 677 M. B. De Groot and D. R. Mastbergen. Scour hole slope instability in sandy soil. In *Proceedings*
678 *Third International Conference on Scour and Erosion*, pages 126–127. CURNET, Gouda, The
679 Netherlands, 2006.
- 680 P. L. M. De Vet, B. C. Van Prooijen, and Z. B. Wang. The difference in morphological development
681 between the intertidal flats of the Eastern and Western Scheldt. *Geomorphology*, 281:31–42,
682 2017. doi: 10.1016/j.geomorph.2016.12.031.
- 683 H. J. De Vriend, Z. B. Wang, T. Ysebaert, P. M. J. Herman, and P. Ding. Ecomorphological
684 problems in the Yangtze Estuary and the Western Scheldt. *Wetlands*, 31:1033–1042, 2011. doi:
685 10.1007/s13157-011-0239-7.
- 686 C. Deangeli. The role of slope geometry on flowslide occurrence. *American Journal of Environ-*
687 *mental Sciences*, 3(3):93–97, 2007.
- 688 J. B. Dunbar, V. H. Torrey, and L. D. Wakeley. A case history of embankment failure: geological
689 and geotechnical aspects of the Celotex levee failure, New Orleans, Louisiana. Technical report,
690 US Army Corps of Engineers, Vicksburg, Mississippi, USA, 1999.
- 691 E. Eke, G. Parker, and Y. Shimizu. Numerical modeling of erosional and depositional bank
692 processes in migrating river bends with self-formed width: Morphodynamics of bar push and
693 bank pull. *Journal of Geophysical Research – Earth Surface*, 119:1455–1483, 2014. doi:
694 10.1002/2013JF003020.
- 695 C. T. Friedrichs and D. G. Aubrey. Nonlinear tidal distortion in shallow well mixed estuaries:
696 a synthesis. *Estuarine, Coastal and Shelf Science*, 26(5):521–545, 1988. doi: 10.1016/0272-
697 7714(88)90082-0.
- 698 M. C. Grenfell. *Chute channels in large, sand-bed meandering rivers*. PhD thesis, University of
699 Exeter, 2012.
- 700 H. Hayati and R. D. Andrus. Updated liquefaction resistance correction factors for aged sands.
701 *Journal of Geotechnical and Geoenvironmental Engineering*, 135(11):1683–1692, 2009.

- 702 D. L. Inman, C. E. Nordstrom, and R. E. Flick. Currents in submarine canyon an air-sea-land
703 interaction. *Annual Review of Fluid Mechanics*, 8:275–310, 1976.
- 704 R. Jentink. Opvolging effecten flexibel storten, halfjaarrapportage Plaat van Walsoorden tweede
705 jaar 2015 (in Dutch). Technical report, Rijkswaterstaat Centrale Informatievoorziening, Regio
706 Zuid, Middelburg, 2015. Rapportnummer: 7210A/KR-PVW-2-2015.
- 707 M. C. J. L. Jeuken. *On the morphologic behaviour of the tidal channels in the Westerschelde*
708 *estuary*. PhD thesis, Universiteit Utrecht, 2000.
- 709 M. C. J. L. Jeuken and Z. B. Wang. Impact of dredging and dumping on the stability of ebb-flood
710 channel systems. *Coastal Engineering*, 57, 2010. doi: 10.1016/j.coastaleng.2009.12.004.
- 711 M. G. Kleinhans. Sorting out river channel patterns. *Progress in Physical Geography*, 34:287–326,
712 2010. doi: 10.1177/0309133310365300.
- 713 M. G. Kleinhans, F. Schuurman, W. Bakx, and H. Markies. Meandering channel dynamics in
714 highly cohesive sediment on an intertidal mud flat in the Westerschelde estuary, the Netherlands.
715 *Geomorphology*, 105:261–276, 2009. doi: 10.1016/j.geomorph.2008.10.005.
- 716 R. L. Laury. Stream bank failure and rotational slump: preservation and significance in the geologic
717 record. *Geological Society of America Bulletin*, 82:1251–1266, 1971.
- 718 LCEP. Lower Columbia Digital Terrain Model. online available, 2010. URL
719 <http://www.estuarypartnership.org/lower-columbia-digital-terrain-model>.
720 last accessed 01/03/2017.
- 721 J. R. F. W. Leuven, T. De Haas, L. Braat, and M. G. Kleinhans. Topographic forcing of tidal sand
722 bar patterns for irregular estuary planforms. *Earth Surface Processes and Landforms*, Subm.
723 doi: 10.1002/esp.4166.
- 724 D. R. Lowe. Subaqueous liquefied and fluid sediment flows and their deposits. *Sedimentology*, 23
725 (3), 1976. doi: 10.1111/j.1365-3091.1976.tb00051.x.
- 726 K. Marcoe and S. Pilson. Habitat change in the Lower Columbia River and Estuary, 1870-2011.
727 Technical report, Lower Columbia Estuary Partnership, 2013. EPA final report.

- 728 D. R. Mastbergen. Oeverstabiliteit bij verdieping waterbodems: Rekenmodel HMBreach (in
729 Dutch). Technical report, Delft Cluster, 2009.
- 730 D. R. Mastbergen and R.A. Schrijvershof. Sedimentatiepatronen Plaat van Walsoorden na plaatval
731 22 juli 2014 (in Dutch). Technical report, Deltares, 2016. Deltares.
- 732 D. R. Mastbergen and J. H. Van den Berg. Breaching in fine sands and the generation of sus-
733 tained turbidity currents in submarine canyons. *Sedimentology*, 50(4):625–637, 2003. doi:
734 10.1046/j.1365-3091.2003.00554.x.
- 735 D. R. Mastbergen, G. A. Van den Ham, M. Cartigny, A. Koelewijn, M. De Kleine, J. Hizett,
736 M. Azpiroz, and A. Vellinga. Multiple flow slide experiment in the Westerschelde Estuary,
737 The Netherlands. In Geoffroy Lamarche, Joshu Mountjoy, Suzanne Bull, Tom Hubble, Sebas-
738 tian Krastel, Emily Lane, Aaron Micallef, Lorena Moscardelli, Christof Mueller, Ingo Pecher,
739 and Susanne Woelz, editors, *Submarine Mass Movements and Their Consequences, 7th Int.*
740 *Symp*, volume 41 of *Advances in Natural and Technological Hazards Research*, pages 241–249,
741 Wellington, New Zealand, 2016. Springer International Publishing. doi: 10.1007/978-3-319-
742 20979-1.
- 743 S. M. Olson and T. D. Stark. Liquefied strength ratio from liquefaction flow failure case histories.
744 *Canadian Geotechnical Journal*, 39:629–647, 2002. doi: 10.1139/T02-001.
- 745 H. H. Savenije. Prediction in ungauged estuaries: an integrated theory. *Water Resources Research*,
746 51(4):2464–2476, 2015. doi: 10.1002/2015WR016936.
- 747 F. Schuurman, M. G. Kleinhans, and W. A. Marra. Physics-based modeling of large braided sand-
748 bed rivers: bar pattern formation, dynamics, and sensitivity. *Journal of Geophysical Research –*
749 *Earth Surface*, 118:2509–2527, 2013. doi: 10.1002/2013JF002896.
- 750 D. A. Shuttle and M. G. Jefferies. Dimensionless and unbiased CPT interpretation in sand. *Inter-*
751 *national Journal for Numerical and Analytical Methods in Geomechanics*, 22:351–391, 1998.
- 752 F. Silvis and M. B. De Groot. Flow slide in the Netherlands: experience and engineering practice.
753 *Canadian Geotechnical Journal*, 32:1086–1092, 1995. doi: 10.1139/t95-107.

- 754 A. Simon and A. J. C. Collinson. Quantifying the mechanical and hydrologic effects of riparian
755 vegetation on streambank stability. *Earth Surface Processes and Landforms*, 27(5):527–546,
756 2002. doi: 10.1002/esp.325.
- 757 T. Stoutjesdijk, D. R. Mastbergen, and M. B. De Groot. Stormvloedkering Oosterschelde: ont-
758 twikkelingontgrondingskuilen en stabiliteit bodembescherming, Deelrapportage Hellinginsta-
759 biliteit (in Dutch). Technical report, Deltares, 2012.
- 760 T. P. Stoutjesdijk. Handboek zettingsvloeiing (in Dutch). Technical report, Rijkswaterstaat, Dienst
761 Weg- en Waterbouwkunde, 1994.
- 762 T. P. Stoutjesdijk, M. B. De Groot, and J. Lindenberg. Flow slide prediction method: influence of
763 slope geometry. *Canadian Geotechnical Journal*, 35:43–54, 1998.
- 764 TNO. DINO Database, GeoTOP version 1 release 3, 2016. URL
765 <https://www.dinoloket.nl/ondergrondmodellen>.
- 766 V. H. Torrey. Flow slides in Mississippi riverbanks. In C. R. Thorne, S. R. Abt, B. J. Barendt,
767 S. T. Maynard, and K. W. Pilarczyk, editors, *River, Coastal and Shoreline Protection-Erosion*
768 *Control. Using Riprap and Armourstone*, pages 361–377. Wiley, Chichester, 1995.
- 769 W. I. Van de Lageweg, W. M. Van Dijk, A. W. Baar, J. Rutten, and M. G. Kleinhans. Bank pull
770 or bar push: What drives scroll-bar formation in meandering rivers? *Geology*, 42(4):319–322,
771 2014. doi: 10.1130/G35192.1.
- 772 J. H. Van den Berg, A. Van Gelder, and D. R. Mastbergen. The importance of breaching as a
773 mechanism of subaqueous slope failure in fine sand. *Sedimentology*, 49(1):81–95, 2002. doi:
774 10.1111/j.1525-139X.2006.00168.x-i1.
- 775 G. A. Van den Ham, M. B. De Groot, and D. R. Mastbergen. A semi-empirical method to assess
776 flow-slide probability. In S. Krastel, J.-H. Behrmann, D. Volker, M. Stipp, C. Berndt, R. Urge-
777 les, J. Chaytor, K. Huhn, M. Strasser, and C. B. Harbitz, editors, *Submarine mass movements*
778 *and their consequences*, volume 37. Advances in Natural and Technological Hazards Research,
779 Springer International Publishing Switzerland, 2014. doi: 10.1007/978-3-319-00972-8.

- 780 M. Van der Wegen and J. A. Roelvink. Reproduction of estuarine bathymetry by means of a
781 process-based model: Western Scheldt case study, the Netherlands. *Geomorphology*, 179:152–
782 167, 2012. doi: 10.1016/j.geomorph.2012.08.007.
- 783 W. M. Van Dijk, F. Schuurman, W. I. Van de Lageweg, and M. G. Kleinhans. Bifurcation instability
784 determines chute cutoff development in meandering gravel-bed rivers. *Geomorphology*, 213:
785 277–291, 2014. doi: 10.1016/j.geomorph.2014.01.018.
- 786 W. M. Van Dijk, A. L. Densmore, R. Sinha, A. Singh, and V. R. Voller. Reduced-complexity
787 probabilistic reconstruction of alluvial aquifer stratigraphy, and application to sedimentary fans
788 in northwestern India. *Journal of Hydrology*, 2016. doi: 10.1016/j.jhydrol.2016.08.028.
- 789 A. Van Duinen, A. Bezuijen, G. Van den Ham, and V. Hopman. Field measurements to investigate
790 submerged slope failures. In S. Krastel, J.-H. Behrmann, D. Volker, M. Stipp, C. Berndt, R. Urge-
791 les, J. Chaytor, K. Huhn, M. Strasser, and C. B. Harbitz, editors, *Submarine Mass Movements*
792 *and Their Consequences*, volume 37, pages 13–21. Advances in Natural and Technological Haz-
793 ards Research, Springer International Publishing Switzerland, 2014. doi: 10.1007/978-3-319-
794 00972-8.
- 795 C. Van Rhee and A. Bezuijen. The breaching of sand investigated in large-scale model tests. In
796 *Proceeding International Conference Coastal Engineering*, volume 3, pages 2509–2519. ASCE,
797 Copenhagen, 1998.
- 798 S. Van Schaick. Morphological development after the July 2014 flow slide on the tidal flat of
799 Walsoorden in the Western Scheldt. Master’s thesis, Delft University of Technology, November
800 2015.
- 801 VBA. Analyse historische plaatvallen oostelijk deel Westerschelde (in Dutch). Nota, International
802 Marine & Dredging Consultants, 2016.
- 803 Z. B. Wang and J. Winterwerp. Impact of dredging and dumping on the stability of ebb-flood
804 channel systems. In *Proceeding of the 2nd IAHR symposium on River, Coastal and Estuarine*
805 *Morphodynamics*, pages 515–524, Obihiro, Japan, 2001. IAHR.

- 806 WBI. Regeling veiligheid primaire waterkeringen 2017: Bijlage III Sterkte en veiligheid (in
807 Dutch), 2017.
- 808 N. Wiegmann, R. Perluka, S. Oude Elberink, and J. Vogelzang. Vaklodingen: de inwintechnieken
809 en hun combinaties: vergelijking tussen verschillende inwintechnieken en de combinaties ervan
810 (in Dutch). Technical report, Technical Report Adviesdienst Geo-Informatica en ICT (AGI)
811 Delft, 2005.
- 812 M. H. Wilderom. *Tussen afsluitdammen en deltadijken, I Noord-Beveland (in Dutch)*. Rijkswater-
813 staat, 1961.
- 814 M. H. Wilderom. *Tussen afsluitdammen en deltadijken, II Noord-Zeeland (in Dutch)*. Rijkswater-
815 staat, 1964.
- 816 M. H. Wilderom. *Tussen afsluitdammen en deltadijken, III Midden-Zeeland (in Dutch)*. Rijkswa-
817 terstaat, 1968.
- 818 M. H. Wilderom. Plaatvallen (in dutch). *OTAR*, 57(7):288–305, 1972.
- 819 M. H. Wilderom. *Tussen afsluitdammen en deltadijken, IV Zeeuwsch Vlaanderen (in Dutch)*.
820 Rijkswaterstaat, 1973.
- 821 M. H. Wilderom. Resultaten van het vooroveronderzoek langs de Zeeuwse stromen (in Dutch).
822 Technical report, Rijkswaterstaat, 1979. Nota 75.2.
- 823 W. F. Willingham. Army engineers and the development of Oregon: A history of the Portland
824 District. Technical report, U.S. Army Corps of Engineers, 1983.
- 825 L. Xie, H. Lei, Y. Yu, and X. Sun. Incipient motion of riverbanks sediments with out-
826 flow seepage. *Journal of Hydraulic Engineering*, 135, 2009. doi: 10.1061/(ASCE)0733-
827 9429(2009)135:3(228).

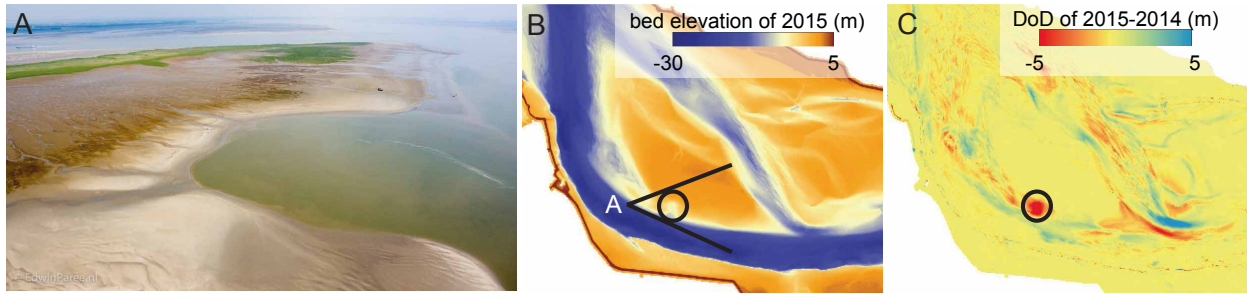


Figure 1: Example of a shoal margin collapse in the Western Scheldt Estuary. A) Aerial view of the tidal flat of Walsoorden after the July 2014 collapse (photo courtesy Edwin Parez, RWS). B) Bathymetry data ('vakkodingen') from the tidal flat of Walsoorden for 2015. C) Example DEM of Difference (DoD) between consecutive years used to identify location, geometry and shape of shoal margin collapses, here for the case shown in A and B.

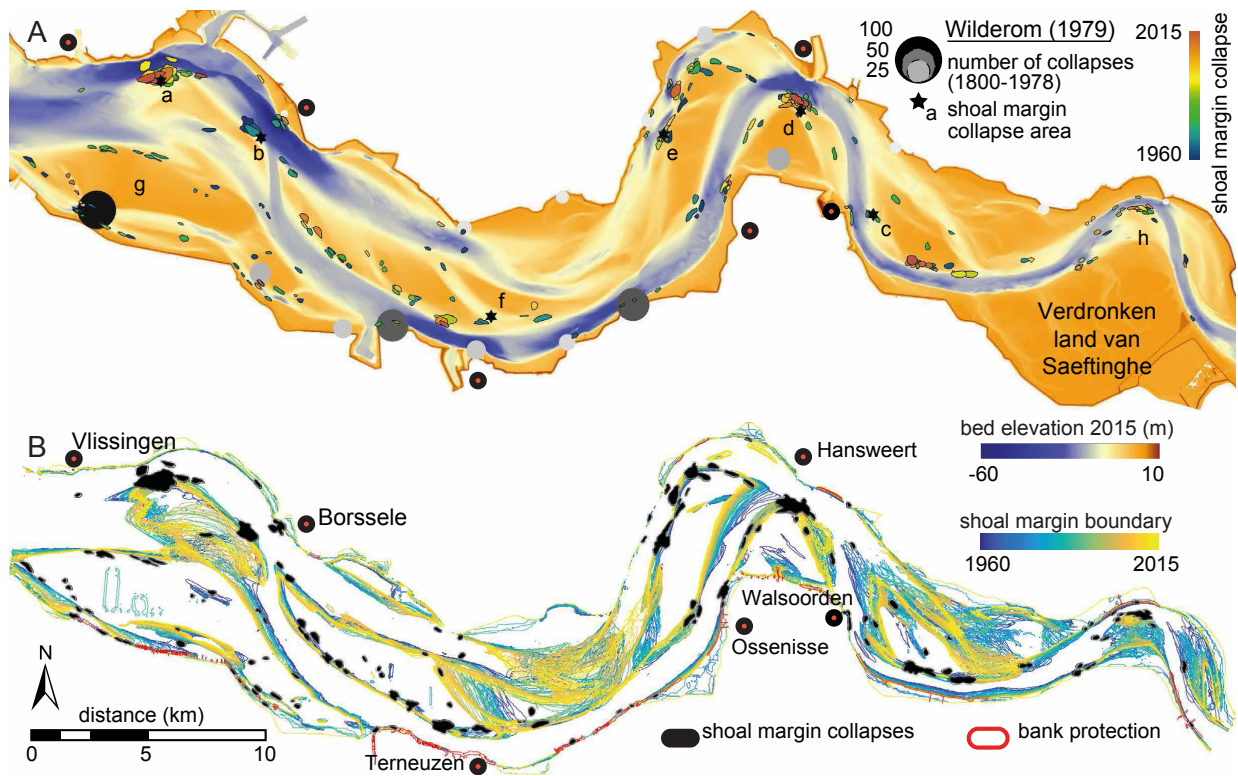


Figure 2: Shoal margin collapses and migration in the Western Scheldt in the period 1960-2015. A) Digital Elevation Model (DEM) for the Western Scheldt with dominant locations for stretches with bank and shoal margin collapses identified by Wilderom (1979), and shoal margin collapses identified in this study. Note symbols a-h are given in the discussion section. B) Shoal margin location at mean bed elevation per year for the period 1960-2015 illustrates that collapses occur mostly along laterally immobile shoal margin locations.

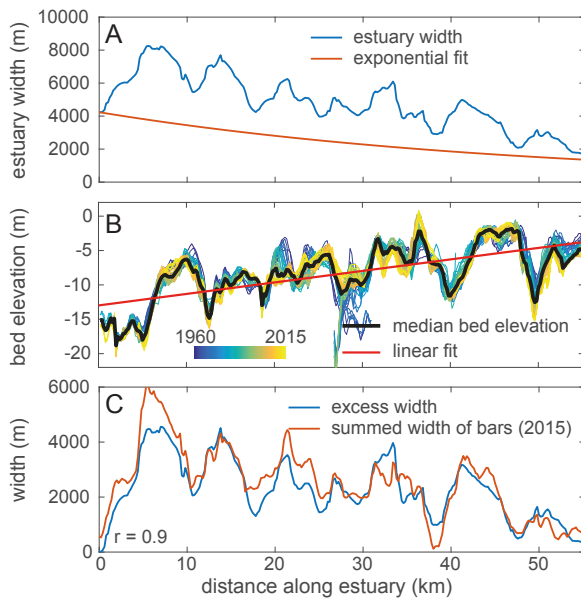


Figure 3: Occurrence of shoals related to estuary width. A) Estuary width based on planform polygons for the Western Scheldt (modified from Leuven et al., Subm). An exponential function is fitted on the width between the mouth and the upstream minimum river width. B) Summed width of shoals is defined as the length over which the elevation exceeds a linear fit on the along-channel median bed elevation (Leuven et al., Subm). A single fit was used for the period 1960-2015, because variations in median bed level were minor. C) Excess width was calculated as the estuary width minus the exponential width and compared to the measured summed width of shoals derived from bathymetries (Figure 3B). The r-value indicates the correlation coefficient.

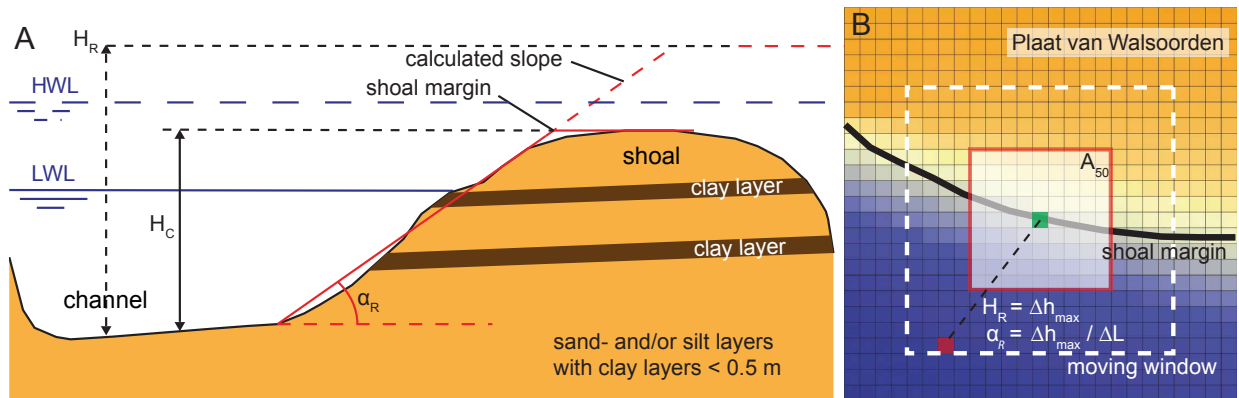


Figure 4: Measurements required for bank safety assessment and probability of occurrence of a shoal margin collapse. A) Existing transect method where relative slope height (H_R , equation 4) or channel height (H_C , equation 5) and relative slope angle (α_R , equations 4-5) for the bank safety assessment are calculated across the channel (modified after WBI, 2017). LWL stands for Low Water Level, and HWL for High Water Level. B) Our modified method to determine relative slope height and relative slope angle from the DEMs. A window is chosen that has the same size as the median shoal margin collapsed area (A_{50}), and calculated within the window is the maximum relative slope height and the corresponding relative slope angle in arbitrary direction.

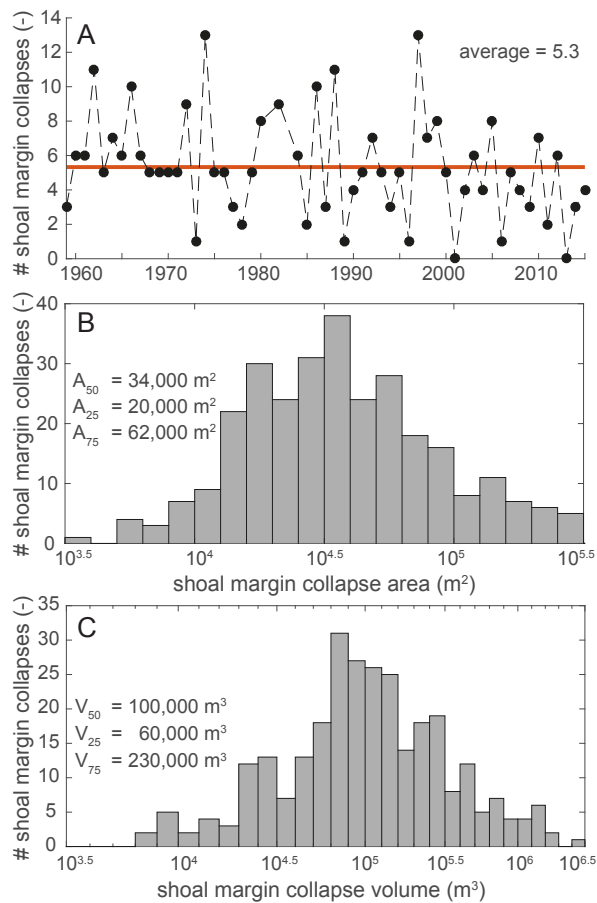


Figure 5: Number, size and volume of shoal margin collapses for the period 1960-2015. A) The yearly average number of shoal margin collapses is 5.3 and decays over the years according to a linear regression of $-0.057\text{years}+7.096$. B) The size of the shoal margin collapses varies from the smallest of $3,000 m^2$ up to $300,000 m^2$, but half of the collapses cover an area between $20,000$ and $62,000 m^2$. C) The volume of the shoal margin collapses varies from $6,000 m^3$ up to $3,000,000 m^3$, whereas the median is about $100,000 m^3$.

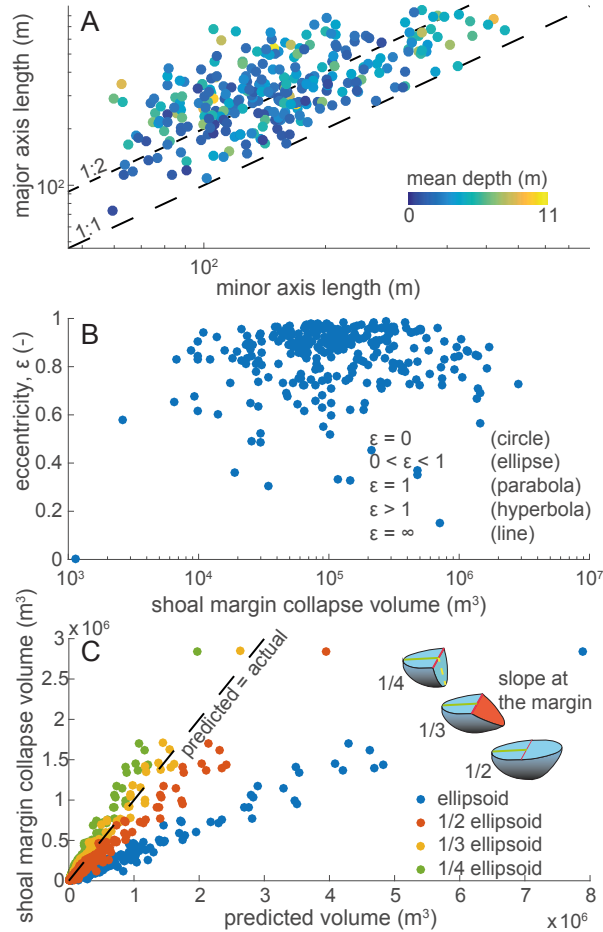


Figure 6: Geometry of all shoal margin collapses. A) The collapses are not rounded shaped, but the major-axis is generally twice the length of the minor axis (equality line indicated). Colors indicate the measured depth of the eroded scar, which is uncorrelated to surface minor and major axis. B) Eccentricity of the collapses indicates that the shoal margin collapses have an ellipse planform shape that is closer to a parabola than to a perfect circle. There is no relation between the shape of the collapse and the volume. C) The 3D-geometrical shape is best predicted by a 1/3 of the volume of a perfect ellipsoid, probably because of the slope at the shoal margin.

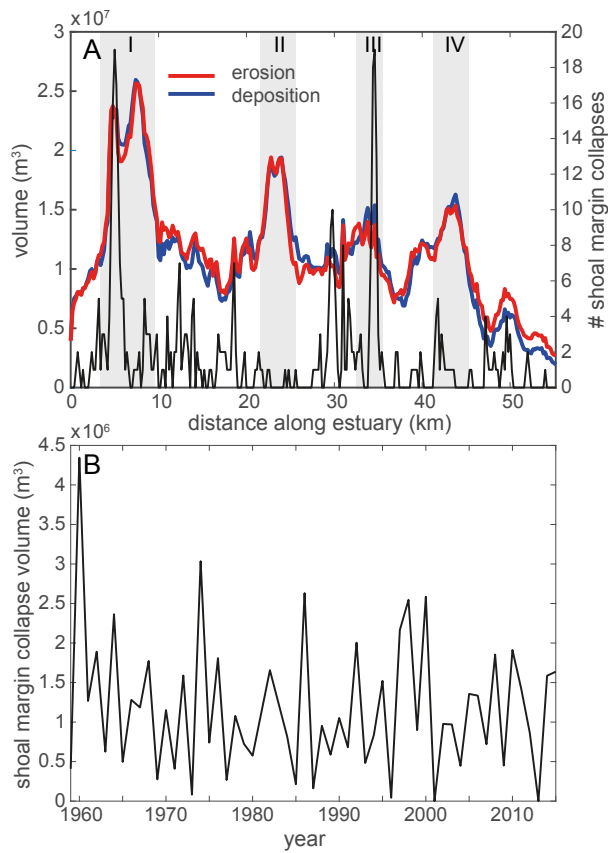


Figure 7: A) Summed erosion and deposition plotted against the summed shoal margin collapse occurrence along the Western Scheldt shows that deposition follows erosion, and several regions (I and III) correspond to high erosion and deposition volumes and shoal margin collapses occurrence, whereas others did not (II and IV). Furthermore, several local peaks within regions with relative less erosion and deposition correspond with the locations of shoal margin collapses, e.g., 14 km, 19 km, 30 km, 31 km, and 50 km. B) Summed sediment volume moved by shoal margin collapses is only a small percentage (2%) of the total eroded sediment volume in Figure 7A.

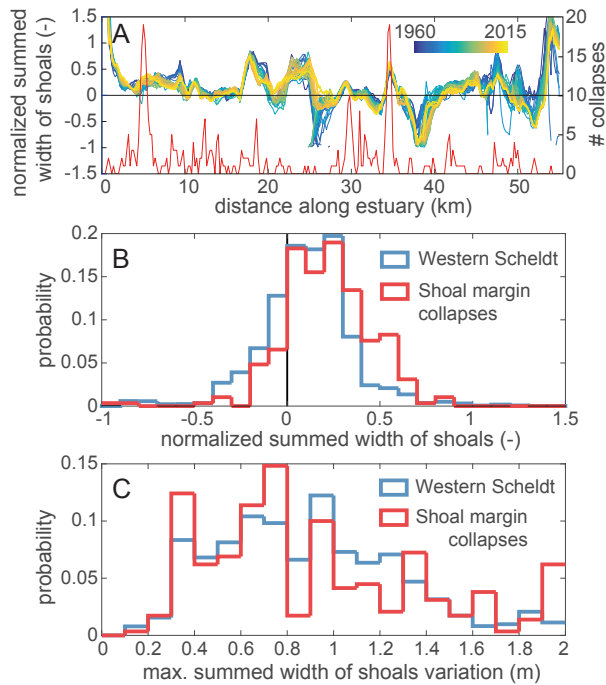


Figure 8: Correlation between variation in summed width of shoals relative to excess estuary width and occurrence of shoal margin collapses. A) Normalized summed width of shoals plotted against the shoal margin collapse locations along the Western Scheldt. Note that the highest peaks in the number of shoal margin collapses correspond to locations with normalized summed width of shoals greater than 0, but not all locations where normalized summed width of shoals is larger than 0 have excessive shoal margin collapses. B) Distribution of the probability of the normalized summed width of shoals shows that for shoal margin collapses the value is mostly above 0 and higher than for the value of the entire Western Scheldt. Note that most collapses occur at locations with a value large than 0, but shoal margin collapses do also occur for locations with values less than 0. C) The distribution of the variation in summed width of shoals, i.e., migration rate, shows no significant difference between locations with and without shoal margin collapses in the Western Scheldt.

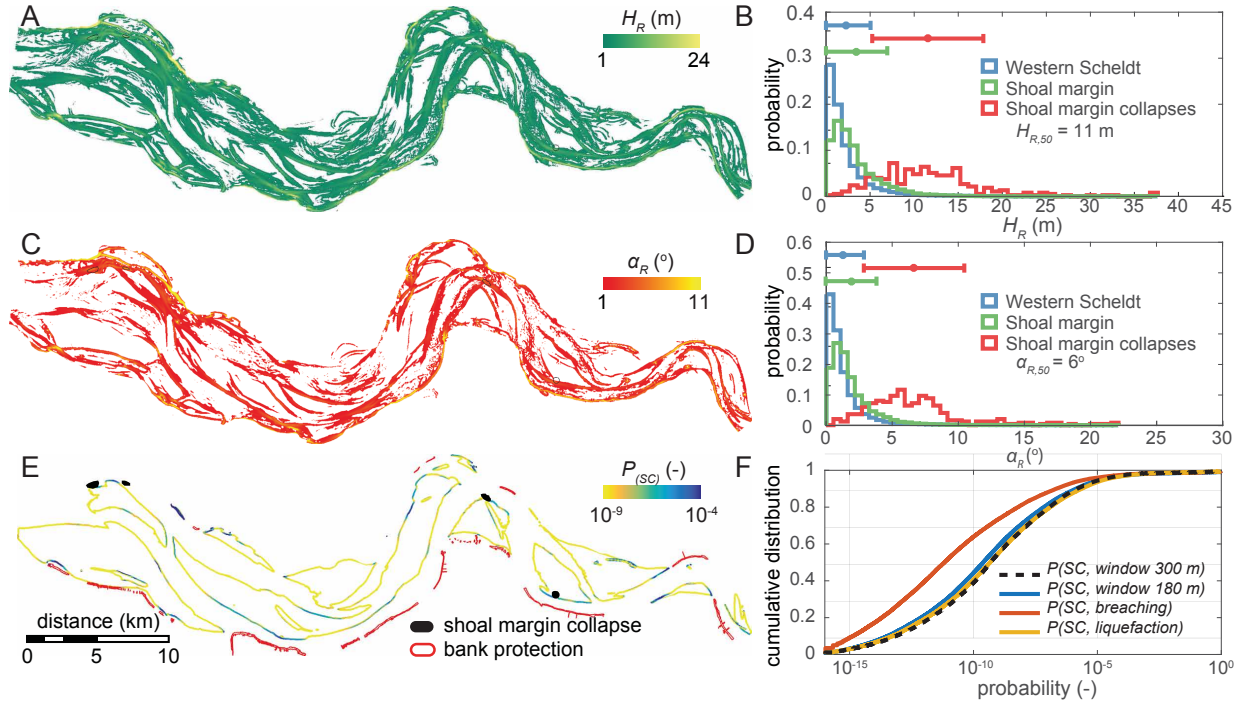


Figure 9: Example of predicted probability of shoal margin collapses. A) H_R map shows the highest slopes at the outer banks of the estuary for the Western Scheldt in 2015. B) The distribution of H_R for the shoal margin collapse locations shows that the median slope height before the collapse was 11 m, which is about the median water depth of 15 m. C) α_R map shows that the steepest slopes are located at the same locations as the highest slopes in Figure 9A for the Western Scheldt in 2015. D) The distribution of α_R for the shoal margin collapse locations illustrates that the angle was 6° , i.e., $\tan(\alpha_r) = 1 : 10$ or $\cot(\alpha_r) = 9.5$. E) The probability map for the shoal margin collapses shows variation in the likelihood of a collapse along the shoal margin. F) The cumulative distribution of the probability maps when assumed formed by breaching or by liquefaction for various failure mechanisms illustrate that flow slides according to equation 4 for liquefaction have considerable a higher probability than flow slides formed by breaching according to equation 5. The combined probability of equation 7 shows that an increasing window size does not increase the probabilities significantly, because of the inverse response of the relative slope angle by an increase of the relative slope height.

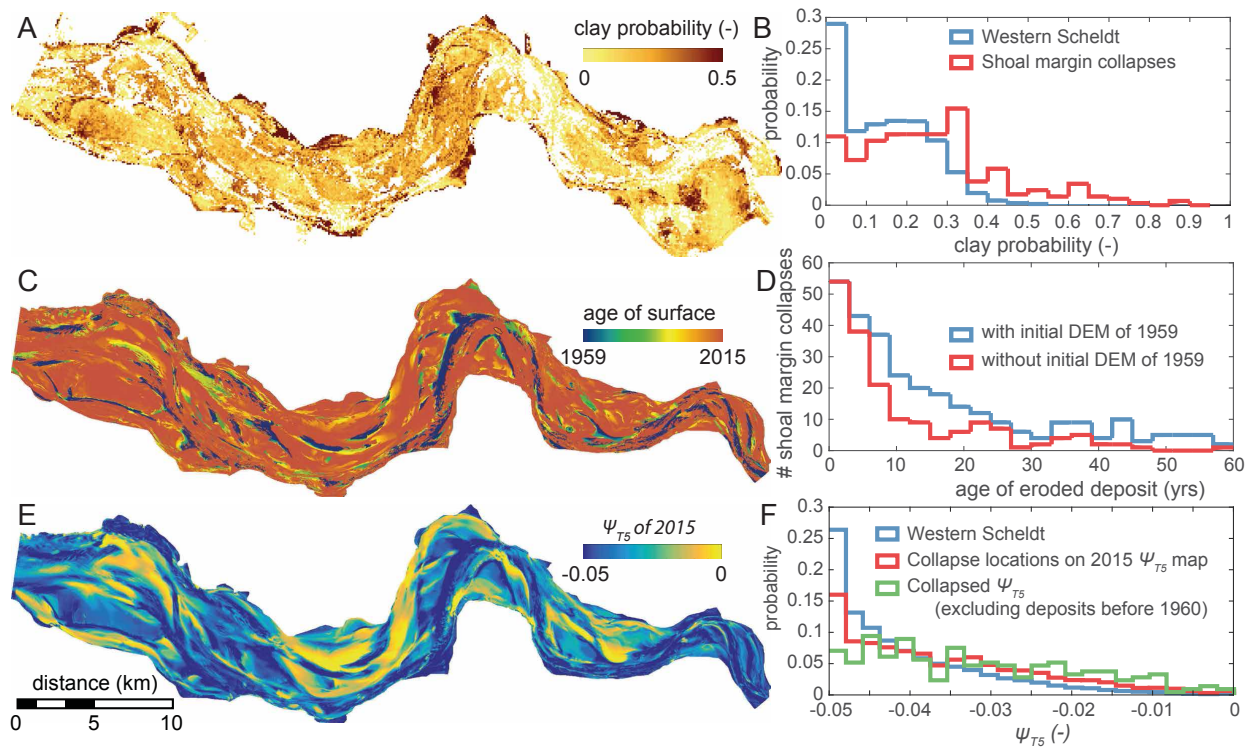


Figure 10: Test of dependence of collapse locations with maps of clay layer (Fr_{clay}) and state parameter (Ψ_{T5}). A) Clay probability distribution in the Western Scheldt according to GeoTOP model (TNO, 2016). B) Distribution of the clay probability of the Western Scheldt and shoal margin collapse locations illustrates a minor shift of the probability distribution for locations with collapses, which indicates a minor influence of clay content. C) Age of the surface deposit calculated from consecutive bathymetry data shows that sediment on the shoals is relative young. D) Age distribution for the shoal margin collapse locations illustrates that the age of the eroded deposit for 50% of the collapses was younger than 10 yrs. E) Assumed state parameter (ψ) map based on a linear regression of the age for the top 5 m deposit. F) The distribution of the state parameter shows that for the shoal margin collapse locations the probability is different than the overall Western Scheldt distribution of the state parameter. Note that we excluded shoal margin collapse locations that eroded sediments deposited before 1959.

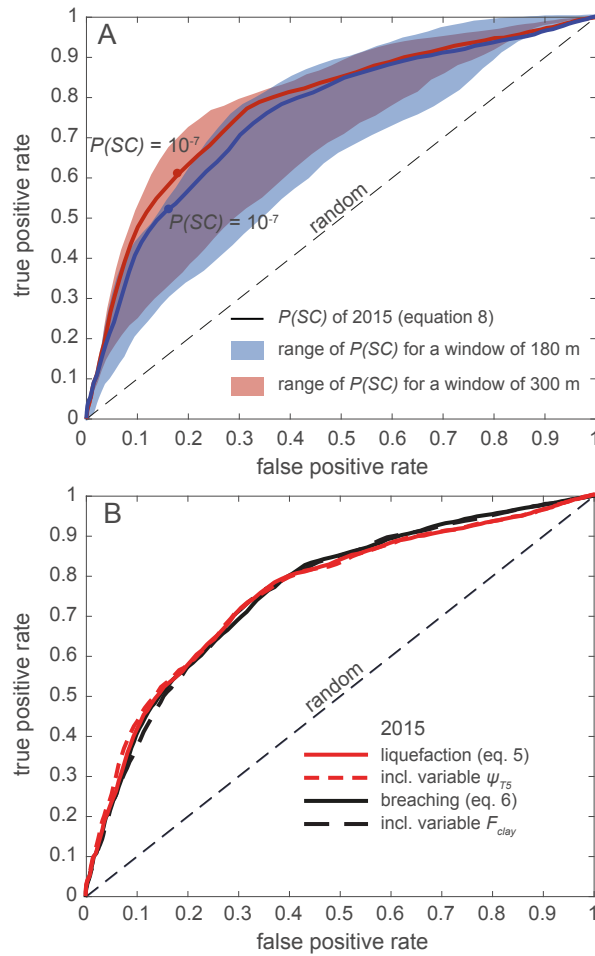


Figure 11: The Receiver Operator Characteristic (ROC) curve, i.e., the false positive rate (FPR) versus the true positive rate (TPR), shows that the predicted probabilities by equation 6 are better than simple randomly selecting shoal margin locations. A) The lower probabilities by a large window size (Figure 9F) lead to an improved prediction indicated by the ROC curve. At a probability value of 10^{-7} the true positive rate is twice as large as the false positive rate and at least 50% of the shoal margin collapse locations are predicted. B) Receiver Operator Characteristic (ROC) curve for the 2015 situation shows that with including a spatial Ψ_{T5} or $F_{r_{clay}}$ does not improve the prediction for liquefaction or breaching, respectively.

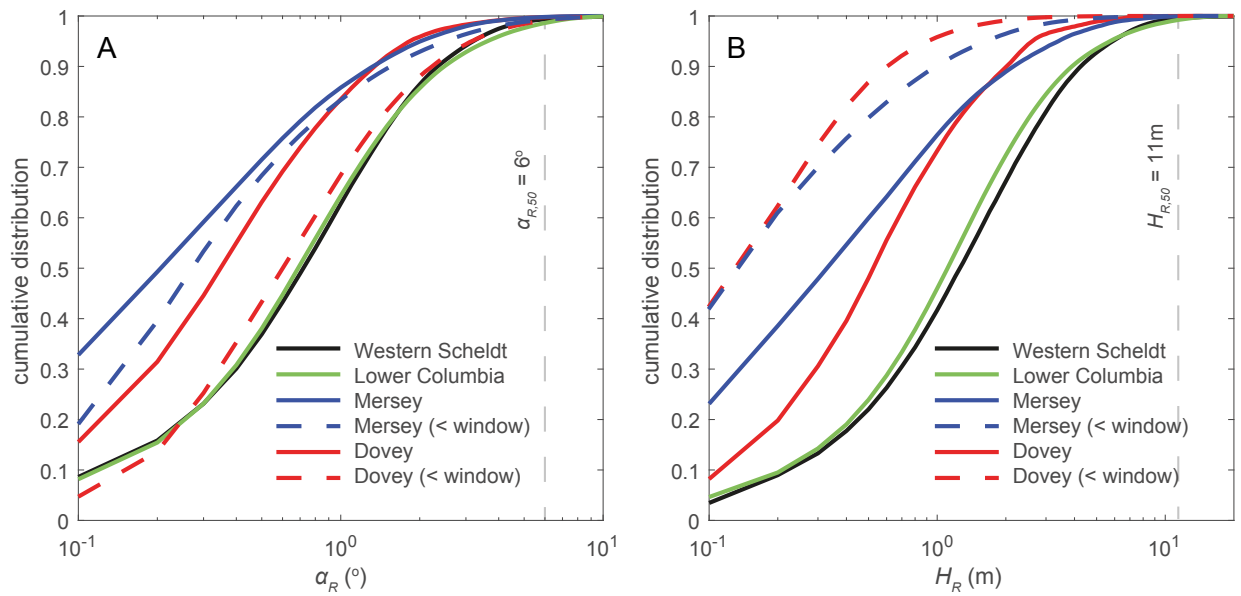


Figure 12: Cumulative distribution of α_R and H_R for various estuaries. A) The Western Scheldt and the Lower Columbia show steeper slopes than the Dovey and Mersey. B) The Western Scheldt and the Lower Columbia have also higher slopes than the Dovey and Mersey. Note that with decreasing the window size, because the smaller estuary size of the Dovey and Mersey and assuming smaller collapses, α_R is generally steeper whereas H_R decreases instead.